Journal of Materials Chemistry A

Cite this: J. Mater. Chem. A, 2019, 7, 10346

Oxygen-deficient titanium dioxide as a functional host for lithium–sulfur batteries†

Hong-En Wang,[a] Kaili Yin,[a] Ning Qin,[c] Xu Zhao,[d] Fan-Jie Xia,[a] Zhi-Yi Hu,[a] Guanlun Guo,*[f] Guozhong Cao*[e] and Wenjun Zhang*[b]

Received 12th February 2019
Accepted 18th March 2019

DOI: 10.1039/c9ta01598a

rsc.li/materials-a

The shuttling of polysulfides with sluggish redox kinetics has severely retarded the advancement of lithium–sulfur (Li–S) batteries. In this work oxygen-deficient titanium dioxide (TiO_2) has been investigated as a novel functional host for Li–S batteries. Experimental and first-principles density functional theory (DFT) studies reveal that oxygen vacancies ($V_O^{\cdot\cdot}$) help to reduce polysulfide shuttling and catalyze the redox kinetics of sulfur/polysulfides during cycling. Consequently, the resulting TiO_2/S composite cathode manifests superior electrochemical properties in terms of high capacity (1472 mA h g^{-1} at 0.2C), outstanding rate capability (571 mA h g^{-1} at 2C), and excellent cycling properties (900 mA h g^{-1} over 100 cycles at 0.2C). The present strategy offers a viable way through vacancy engineering for the design and optimization of high-performance electrodes for advanced Li–S batteries and other electrochemical devices.

Introduction

Lithium–sulfur (Li–S) batteries (LSBs) have been considered as a promising next-generation electrochemical energy storage system due to their ultrahigh theoretical energy density (2600 W h kg^{-1}), abundant sulfur sources in the earth's crust with low-cost, and environmental benignity.[1–3] However, the electrochemical performance of LSBs has been largely affected by the shuttling of lithium polysulfide intermediates (Li_2S_x, $3 < x \leq 8$) which are easily soluble in ether-based electrolytes.[4] Thus far, various approaches have been reported to address the intractable issue of polysulfide shuttling, *e.g.*, through modifying separators,[5] adding interlayers,[6,7] optimizing the binder[8,9] and electrolyte compositions,[10,11] and manipulating Li-anodes to enhance their stability.[12] Nevertheless, due to the changing polarities of polysulfides during discharge/charge processes, these approaches could suppress their shuttling to a certain extent only. There is still considerable space for improving the performance of LSBs before they could be used practically.

Regulating the composition and structure of the cathode is another useful strategy to tackle the problem of polysulfide shuttling.[13–15] Particularly, cathodes based on various carbon nanostructures have been reported, such as meso-/microporous carbon,[16,17] hollow carbon,[18,19] graphene,[20] carbon nanotubes,[20,21] and their composites.[22,23] In general, due to the intrinsically non-polar nature of these carbon materials, they could not mitigate the shuttling of polysulfides alone.[24,25] Polar compounds, such as transition metal oxides,[26–29] sulfides,[30–33] selenides,[34] carbides,[35] nitrides,[36–41] and phosphides,[42,43] have thus drawn increasing attention as potential cathode hosts because of their stronger chemical affinity to polysulfides. Among these polar compounds, TiO_2 has manifested a high affinity to polysulfides due to the strong Lewis acid–base interaction between the empty 3d orbitals of Ti^{4+} and electron-rich polysulfide anions (S_x^{2-}).[44,45] Moreover, TiO_2 could promote the redox conversion of polysulfides during charge/discharge.[46] However, the electrical conductivity of TiO_2 and its interaction with polysulfides need to be further improved for application in practical LSBs.

Hybridizing TiO_2 with graphene,[47,48] carbon nanotubes,[49] porous carbon matrices[50] or MXenes[51] enabled enhanced electrical conductivity of TiO_2-based electrodes used in LSBs, albeit multi-step and complicated processing were required, and the uneven distribution of respective components in the final composites was another problem to be solved. Thus, rational design and fabrication of TiO_2/C composites with controlled

[a]State Key Laboratory of Advanced Technology for Materials Synthesis and Processing, Wuhan University of Technology, Wuhan 430070, China
[b]Centre of Super Diamond & Advanced Films (COSDAF), Department of Materials Science and Engineering, City University of Hong Kong, HKSAR, China. E-mail: apwjzh@cityu.edu.hk
[c]Department of Materials Science and Engineering, Southern University of Science and Technology, Shenzhen 518055, China
[d]Institute of Chemical Materials, China Academy of Engineering Physics, Mianyang 621900, China
[e]Department of Materials Science and Engineering, University of Washington, Seattle, WA 98195, USA. E-mail: gzcao@u.washington.edu
[f]Hubei Key Laboratory of Advanced Technology for Automotive Components, Wuhan University of Technology, Wuhan 430070, China. E-mail: glguo@whut.edu.cn

† Electronic supplementary information (ESI) available: Experimental section, scheme for materials synthesis, digital photos, SEM images, N_2 adsorption isotherms, TG curves, additional XPS spectra, Raman spectra, additional XRD and TEM data, additional CV and GCD curves, additional computational details, UV-vis spectra, and performance comparison tables. See DOI: 10.1039/c9ta01598a

composition and component distribution as sulfur hosts by facile reaction routes are still desired for high-performance LSBs. Alternatively, incorporation of oxygen vacancies ($V_O^{\cdot\cdot}$) in TiO_2 has been proposed as an effective route to boost its electrical conductivity as $V_O^{\cdot\cdot}$ can serve as a shallow donor to increase the free charge carrier concentration.[52] Several oxygen-deficient TiO_2 nanostructures with different polymorphs have been demonstrated to be able to deliver excellent rate capability for $Li^+/Na^+/Mg^{2+}$ storage.[53–57] Moreover, recent work has also suggested that the introduction of sulfur or oxygen vacancies could improve the chemical interactions of the cathode hosts with polysulfides and enhance the cycling stability of LSBs,[30,33,58,59] though the mechanism behind this was still unclear.

Herein, we report oxygen-deficient TiO_2 as a cathode host for LSBs. Based on experimental observations and calculations by first-principles density functional theory (DFT), the $V_O^{\cdot\cdot}$ enhanced the affinity of TiO_2 towards polysulfides and simultaneously catalyzed their redox conversion by propelling the electron/Li^+ transport on the vacancy-enriched surface. As a result, the TiO_2/S composite cathode exhibited superior electrochemical performance. The presented methodology in this work may lead to new ideas on the design and exploration of novel nanocomposite electrodes with rationally engineered structural defects for next-generation electrochemical energy storage and conversion devices.

Results and discussion

The schematic fabrication procedure of mesoporous TiO_2 samples is shown in Scheme 1. First, amorphous TiO_2–oleylamine (TiO_2/OA) hybrid spheres were prepared by a sol–gel process (Scheme 1a). Then, the TiO_2/OA spheres were converted into mesoporous anatase TiO_2 spheres covered by trace OA by a hydrothermal treatment in an ethanol/H_2O mixture (Scheme 1b). Finally, the mesoporous anatase TiO_2/OA spheres were annealed in Ar or air, leading to the formation of mesoporous oxygen-deficient anatase spheres (denoted as TiO_2–Ar, Scheme 1c) or oxygen vacancy-free anatase (TiO_2–air, Scheme 1d), respectively. Compared to white TiO_2–air, the TiO_2–Ar sample is dark-brown in colour (Fig. S1†).

Scanning electron microscopy (SEM) images show that both samples consist of mesoporous spheres (1–2 μm in diameter) composed of interconnected particles of ~10 nm (Fig. S2†). Such porous nanostructures possess high specific surface areas and pore volumes (118 $m^2 g^{-1}$ and 0.58 $cm^3 g^{-1}$ for TiO_2–Ar; 121 $m^2 g^{-1}$ and 0.6 $cm^3 g^{-1}$ for TiO_2–air), as determined using N_2 sorption isotherms by the Brunauer–Emmett–Teller (BET) method (Fig. S3a and Table S1†). The interconnection of nanocrystals yields a narrow pore distribution with sizes centering at 9.4 nm (for TiO_2–Ar) and 10.6 nm (for TiO_2–air) by Barrett–Joyner–Halenda (BJH) analyses (Fig. S4b†).

High-angle annular dark-field scanning transmission electron microscopy (HAADF-STEM) images (Fig. 1a) show that the TiO_2–Ar product contains mesoporous spheres composed of crystalline nanoparticles. The corresponding selected area electron diffraction (SAED) (insets of Fig. 1b and c) patterns present the high degree of crystallinity of the TiO_2 nanoparticles. The high resolution TEM (HRTEM) image (Fig. 1b) reveals that most TiO_2 nanoparticles have clean surfaces, suggesting a low carbon content. The weight fraction of carbon has been further determined to be ~2 wt% by thermogravimetric (TG) analyses (Fig. S4a†). The corresponding energy-dispersive X-ray (EDX) elemental maps and overlay (Fig. 1d–f) validate that C and Ti are homogeneously distributed throughout the whole mesoporous sphere.

To obtain more structural information, X-ray diffraction (XRD), electron paramagnetic resonance (EPR), X-ray photoelectron spectroscopy (XPS) and Raman characterization were carried out. In Fig. 2a, the XRD patterns of both samples can be readily indexed to the anatase phase (space group $I4_1/amd$, JCPDS no. 21-1272) with good crystallinity.[60] Furthermore, the XRD patterns indicate that TiO_2–Ar could have a smaller crystal size than TiO_2–air. It is very likely that the smaller grain size

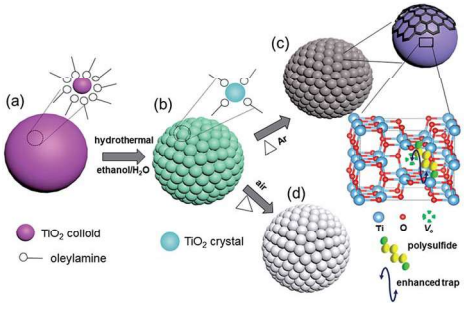

Scheme 1 Synthesis process of mesoporous oxygen-deficient TiO_2. (a) amorphous TiO_2/oleylamine hybrid spheres, (b) mesoporous TiO_2 with minor oleylamine capping on the surface, (c) mesoporous oxygen-deficient TiO_2 bonded with minor carbon, and (d) mesoporous TiO_2.

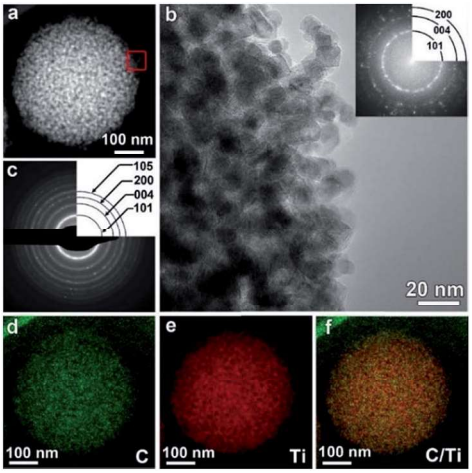

Fig. 1 TEM and EDX analysis of the TiO_2–Ar sample. (a) HAADF-STEM image; (b) HRTEM image of the area indicated by the red box in (a), (c) corresponding SAED pattern of the whole area in (a), and (d–f) corresponding EDX elemental maps: C (green), Ti (red) and their overlay.

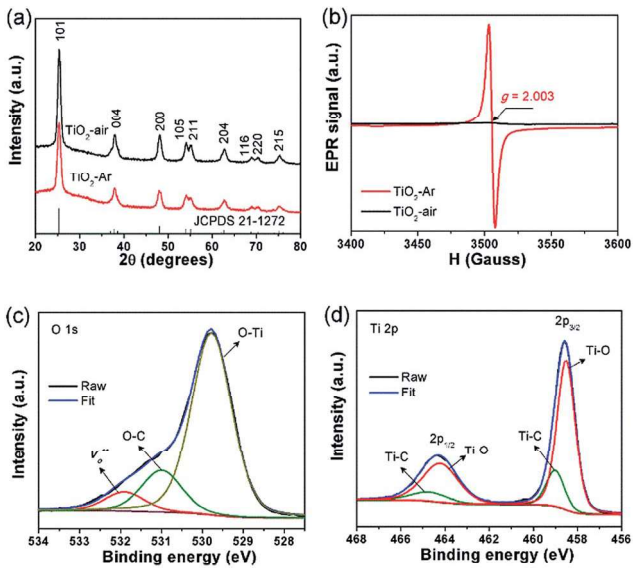

Fig. 2 (a) XRD patterns, (b) room-temperature EPR spectra of TiO_2–Ar and TiO_2–air samples; high-resolution XPS spectra of (c) O 1s and (d) Ti 2p in the TiO_2–Ar/S sample.

(thus a highly exposed surface) of TiO_2–Ar can lead to higher catalytic activity for polysulfide conversion when used in Li–S cells. In Fig. 2b, only one strong EPR signal with a g value of ~2.003 is observed for TiO_2–Ar, corresponding to the presence of $V_O^{\cdot}$ with excess unpaired electrons delocalized.[56,57] The formation of $V_O^{\cdot}$ can be ascribed to the withdrawal of some of the oxygen atoms from the TiO_2 lattice during carbonization of residual oleylamine in Ar. In contrast, no EPR signal is detected in the TiO_2–air sample, implying either the absence of or a very low concentration of $V_O^{\cdot}$. The deconvolution of the O 1s XPS spectrum (Fig. 2c) reveals the presence of lattice O in TiO_2 (529.8 eV), O–C bonding (531 eV) and $V_O^{\cdot}$ at the surface (532 eV).[61] From the areal ratio of $V_O^{\cdot}$ *versus* lattice O, the concentration of oxygen vacancies on the surface can be estimated to be *ca.* 9%. In the deconvoluted Ti 2p XPS spectrum (Fig. 2d), two major bands with binding energies (BEs) at 464.2 eV and 458.5 eV correspond well to the $2p_{1/2}$ and $2p_{3/2}$ components of Ti^{4+} in the TiO_2 lattice.[62] Two shoulder bands with higher BEs at 464.7 and 459 eV can be attributed to the Ti–C bond at the TiO_2/C interface.[56,63] The fitted C 1s spectrum (Fig. S5a†) unravels the presence of sp^2-hybridized C–C bonds (284.8 eV),[64] C–Ti bonds (284.2 eV),[63] C–S bonds (285.5 eV),[62] C–O bonds (286.4 eV) and C=O bonds (288.7 eV).[65] The S 2p XPS spectrum (Fig. S5b†) indicates the existence of S–S bonds (164.71/163.55 eV) in orthorhombic S_8 molecules, S–C bonds (164.95/163.79 eV),[62] and sulfate species from oxidation of surface sulfur (169.43/168.27 eV).[65] The formed Ti–C and C–S bonds at TiO_2/C and C/S interfaces can thus facilitate electron transfer in the TiO_2–Ar/S electrode during electrochemical redox reactions. Raman measurements show more local structural characteristics of the two samples. In Fig. S6,† the Raman spectrum of the TiO_2–air sample suggests that it is phase-pure anatase. Compared to TiO_2–air, the Raman peak intensity of TiO_2–Ar weakens greatly with several peaks almost diminished, suggesting the enhanced electrical conduction enabled by $V_O^{\cdot}$ and carbon species because high conductivity could lower the skin depth of incident photons with reduced Raman scattering intensity.[66] In addition, two characteristic weak bands at 1387 and 1607 cm^{-1} indicate the presence of amorphous carbon species.[38]

The influence of $V_O^{\cdot}$ on the electronic structures of TiO_2 was further studied using first-principles density functional theory (DFT) calculations. Fig. 3a and b show the optimized geometry structures of the anatase supercell without and with $V_O^{\cdot}$, respectively. From the density of states (DOS) analyses, the electronic energy bandgap (E_g) of the TiO_2 supercell has been reduced from 3.011 eV to 2.867 eV after introducing $V_O^{\cdot}$, suggesting that $V_O^{\cdot}$ can enhance the electronic conductivity of TiO_2.[55,57]

Next, sulhas been fur was loaded into mesoporous TiO_2 by a conventional melt-diffusion approach. Compared to polar TiO_2, nonpolar carbon has a higher affinity to nonpolar sulfur as reflected by the smaller contact angle between carbon and melted sulfur (Fig. S7†). Thus, it is deduced that the penetration of sulfur into the TiO_2–Ar sample can be slightly easier than that of TiO_2–air due to the existence of trace nonpolar carbon in TiO_2–Ar. The resultant two composites (denoted as TiO_2–Ar/S and TiO_2–air/S, respectively) retain rough spherical morphologies albeit with greatly reduced mesopores on the surface (Fig. S8†), leading to a sharp reduction of the specific surface area (Fig. S3 and Table S1†). XRD reveals that the loaded sulfur species in both TiO_2 samples (Fig. S9†) crystallize in the orthorhombic phase (space group *Fddd*, JCPDS no. 42-1278).[33] TEM observation discloses that the defective structure (lattice

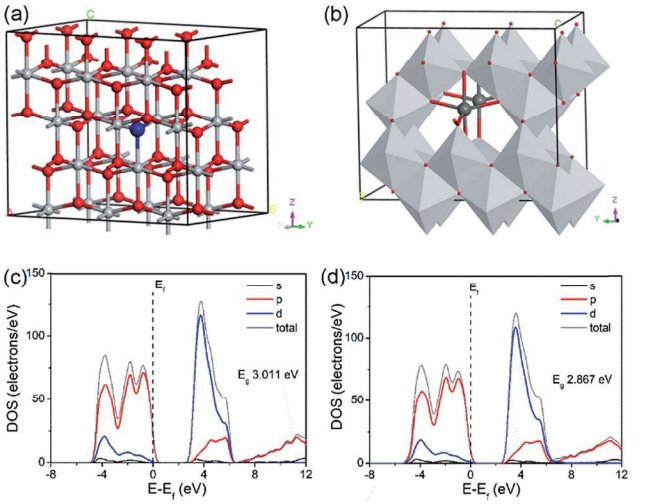

Fig. 3 Crystal and electronic structures of bulk TiO_2 after geometry optimization. (a) Pristine anatase 2 × 3 × 1 supercell shown in ball-and-stick mode (one O atom to be removed in (b) is labelled in blue), (b) anatase 2 × 3 × 1 supercell with one $V_O^{\cdot}$ presented in polyhedral and ball-and-stick mode (the $V_O^{\cdot}$ is formed between two grey Ti atoms); (c and d) calculated total and partial density of states (DOS) of anatase 2 × 3 × 1 supercells without (c) and with one $V_O^{\cdot}$ (d). The grey and red balls in (a and b) represent Ti and O atoms, respectively. E_f in (c and d) represents the Fermi energy level and its position is set at zero.

distortion and $V_o^{\cdot\cdot}$) preserved after sulfur loading into TiO_2–Ar (Fig. S10†).

The electrochemical properties of the resultant TiO_2/S composite electrodes in Li–S cells were evaluated using cyclic voltammetry (CV), galvanostatic charge/discharge (GCD) and electrochemical impedance spectroscopy (EIS) measurements. The CV sweep of the TiO_2–Ar/S electrode (Fig. S11a†) shows that the TiO_2–Ar/S electrode undergoes a two-step reduction reaction during the cathodic scan as suggested by two reduction peaks. The first peak at ~2.3 V corresponds to the reduction of solid S_8 to long-chain soluble Li_2S_x ($4 \leq x \leq 8$), and the second at ~2.1 V represents further reduction from short-chain polysulfides to solid discharge product Li_2S_2/Li_2S.[30] In the following anodic sweep, only one merged oxidation peak appears at around 2.4 V, signifying the re-oxidation of Li_2S/Li_2S_2 to polysulfides and finally to solid sulfur.[30] The rough superimposition of the initial three CV cycles indicates the high electrode reversibility with low loss of active sulfur species. GCD curves of the TiO_2–Ar/S electrode (Fig. S11b†) also exhibit two discharge potential plateaus and one long charge plateau,[31] which agrees with the CV data (Fig. S11a†). In addition, the TiO_2–Ar/S cathode delivers a high initial discharge capacity of 1578 mA h g^{-1} with a utilization of ~94% of the active sulfur species. The exact capacities from the upper-voltage plateau region and lower-voltage region are estimated to be ~401 and ~1177 mA h g^{-1}, respectively. The small deviation of the GCD curves during the first 3 cycles further demonstrates high reversibility.

For comparison, Fig. 4a presents the CV curves of the TiO_2–Ar/S, TiO_2–air/S and bare sulfur electrodes. Clearly, TiO_2–Ar/S exhibits a much larger peak current response during the redox process and a higher reduction peak position (~2.06 V) in the 2nd potential region, followed by a narrow and sharp oxidation peak, suggesting that TiO_2–Ar/S can effectively bind polysulfides and propel their conversion. In the GCD curves (Fig. 4b), both TiO_2–Ar/S and TiO_2–air/S (Fig. 4b) display a similar and lower overpotential (~270 and 280 mV) than that of the bare sulfur electrode (~320 mV) due to the enhanced reaction kinetics with reduced polarization.[67] In addition, the TiO_2–Ar/S cathode delivers the highest discharge capacity of 947 mA h g^{-1}, and the relative capacity contributions from the first upper-voltage and second lower-voltage regions are calculated to be 21% and 35.5%, respectively, higher than those of TiO_2–air/S (14% and 26.5%) and pure sulfur (10.2% and 14.5%). The higher capacity of the TiO_2–Ar/S cathode mainly stems from the enhanced conductivity of the TiO_2–Ar host with $V_o^{\cdot\cdot}$ and carbon decoration.

Rate capability (Fig. 4c) shows that all 3 electrodes possess reduced capacities with increasing current rates from 0.2 to 5C due to increased polarization. At 0.2C, the two TiO_2/S electrodes exhibit a noticeable capacity drop. This phenomenon can be mainly caused by the existence of a few sulfur species outside the mesoporous TiO_2. Note that the pore volume of our two samples is ~0.6 cm^3 g^{-1}, this value is not very large compared to that of some porous carbon nanostructures (>1 cm^3 g^{-1}). Thus, a few sulfur species could reside outside the TiO_2 surface. During discharge/charge, the outside sulfur species could form polysulfides and shuttle, giving rise to considerable capacity loss especially at a low current density (*e.g.*, 0.2C). To solve this issue, it is necessary to further optimize the crystal size and particularly the pore structure (volume) of the mesoporous TiO_2 materials. In addition, additional modification of the surface of the mesoporous TiO_2 spheres, such as coating with highly conducting rGO nanosheets can also improve the cyclability and electronic conductivity of the composite cathode. Nonetheless, the TiO_2–Ar/S cathode can still sustain high reversible capacities of 1591, 999, 712, 571 and 401 mA h g^{-1} at current densities of 0.2, 0.5, 1, 2 and 5C, respectively. After switching the current rate back to 0.5C, a capacity of 770 mA h g^{-1} was restored, demonstrating its good stability. In contrast, the TiO_2–air/S electrode exhibits slightly inferior discharge capacities of 1081, 689, 576, 481 and 333 mA h g^{-1} at 0.2, 0.5, 1, 2 and 5C, respectively. The pure sulfur electrode presents the poorest rate capacities of 711, 413, 341, and 234 mA h g^{-1} at 0.2, 0.5, 1, 2 and 5C, respectively. The rate capability of the TiO_2–Ar/S cathode is also superior to that of some reported sulfur hosts as summarized in Table S2 (ESI†). The electrode kinetics were further investigated by electrochemical impedance spectroscopy (EIS). As shown in Fig. 4d, the Nyquist plots of the three sulfur electrodes all contain two depressed semicircles in high and high-to-medium frequency regions as well as a sloping line in the low frequency region. The first semicircle reflects the formation of

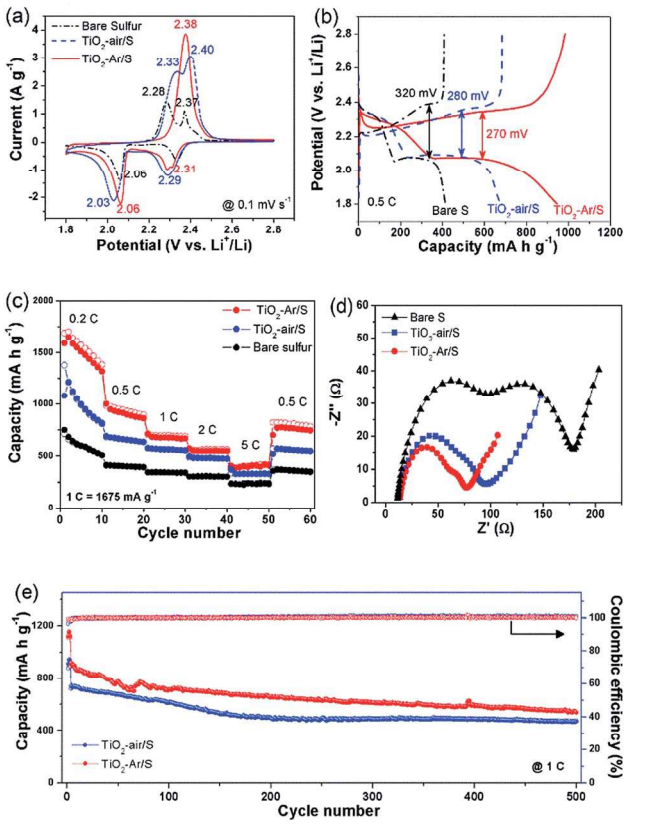

Fig. 4 Electrochemical performance of TiO_2–Ar/S, TiO_2–air/S and bare sulfur electrodes. (a) Cyclic voltammetry, (b) galvanostatic charge–discharge curves, (c) rate capability, (d) electrochemical impedance spectra, and (e) long-term cyclability at 1C (1675 mA g^{-1}).

a passivation film (Li_2S_2/Li_2S) on the lithium anode surface and the second represents the charge transfer resistance (R_{ct}) at the cathode/electrolyte interface;[33] while the sloping line signifies the Li^+ diffusion in the cathode. Apparently, the smallest R_{ct} of the TiO_2–Ar/S electrode compared to that of the TiO_2–air/S and bare sulfur cathode suggests the enhanced electronic/ionic conductivity in the TiO_2–Ar/S electrode, faster charge transfer occurring at the cathode/electrolyte interface and propelled polysulfide redox reactions.[67] The long-term cycling stability tests were also carried out at 0.2C (Fig. S11c†) and 1C (Fig. 4e), respectively. At 0.2C, the TiO_2–Ar/S cathode shows a high initial discharge capacity of ~1472 mA h g^{-1} and retains 900 mA h g^{-1} over 100 cycles with a retention rate of 61%, higher than those of TiO_2–air/S (with an initial capacity of 1470 mA h g^{-1} and retention rate of ~40%) and pristine sulfur (with an initial capacity 894 mA h g^{-1} and retention rate of ~25%). Even at 1C, the TiO_2–Ar/S electrode can manifest a high capacity of 538 mA h g^{-1} over 500 cycles, higher than the 467 mA h g^{-1} for the TiO_2–air/S electrode. The cycling performance of the TiO_2–Ar/S cathode is also superior or comparable to recently reported cathode hosts for Li–S cells, as summarized in Table S3.†

DFT calculations were applied to simulate the adsorption of polysulfides and Li, as well as Li diffusion on the TiO_2 surface. Herein, Li_2S_4 was adopted as a representative polysulfide molecule and its adsorption on the TiO_2 (100) surface was modelled. The simulation results reveal that the adsorption of Li_2S_4 on pristine anatase (100) yields a large binding energy (E_{ad}) of −3.95 eV. Note that the anatase (100) surface has rich two-coordinated O atoms and five-coordinated Ti atoms. After putting Li_2S_4 on the TiO_2 surface, one S atom from Li_2S_4 can bind with one five-coordinated Ti atom on the top surface, forming a S–Ti bond with a bond length of 2.447 Å (Fig. S12a†). In the meantime, the two Li atoms in Li_2S_4 can preferentially bind with their adjacent two-coordinated O atoms from the TiO_2 surface, forming Li–O bonds with bond lengths ranging from 1.899 to 2.018 Å (Fig. S12a and b†).

In comparison, the adsorption of Li_2S_4 on the TiO_2 surface with $V_O^{\cdot}$ has two preferential configurations after geometry optimization. In the first one (Fig. S12c and d†), the two Li atoms tend to coordinate with their adjacent O atoms on the TiO_2 surface to form Li–O bonding; while the one S atom prefers to bind with a four-coordinated Ti atom (adjacent to $V_O^{\cdot}$), showing an increased covalent characteristic with a shorter bond length (2.313 Å) and higher E_{ad} (−4.84 eV) (Fig. S12c†). The formation of multiple Li–O bonds and one S–Ti bond at the Li_2S_4/TiO_2 (100) surface containing $V_O^{\cdot}$ has been further elucidated by the charge density difference plots (Fig. S13a†). In the second configuration, we interestingly notice that the on-top four-coordinated Ti atom (surrounding $V_O^{\cdot}$) can also simultaneously bind two S atoms and a five-coordinated Ti binds another S from Li_2S_4, leading to even stronger chemical adsorption (E_{ad} of −5.23 eV), as shown in Fig. 5 and S12b.† Our calculated E_{ad} values of polysulfide on TiO_2 (100) with and without $V_O^{\cdot}$ are both higher than or comparable to some reported polar host materials, such as Ni_2P (−3.7 eV), Co_2P (−4.18 eV),[42] N-doped graphene (−3.11 eV),[68] and Li_xTiS_2 (−3.4 to −4 eV),[69] suggesting that polysulfides can be tightly adsorbed on the TiO_2 surface *via* interfacial chemical bonding.

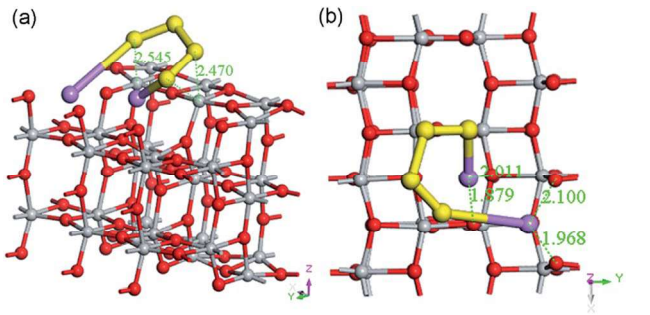

Fig. 5 (a) Tilted and (b) top view of Li_2S_4 adsorbed on the anatase (100) slab surface with $V_O^{\cdot}$ after geometry optimization, suggesting its binding by S–Ti and Li–O bonds between Li_2S_4 and TiO_2. The grey, red, yellow, and pink balls represent Ti, O, S, and Li, respectively.

The high affinity of TiO_2 toward polysulfides with a reduced shuttling effect has been further validated using visual adsorption experiments and ultraviolet-visible (UV-vis) spectra (Fig. S14†) as well as post-mortem analyses of the Li–S cell components (Fig. S15†). In addition, one Li–S bond in Li_2S_4 adsorbed both on anatase (100) and TiO_2 (100) with $V_O^{\cdot}$ has been significantly elongated and breaks due to the strong coordination of Li with multiple surface O atoms, suggesting that the adsorbed Li_2S_4 tends to further decompose into lower-order polysulfides. Given the high electrical conductivity of the TiO_2–Ar promoted by $V_O^{\cdot}$ and Ti–C bonding, the adsorbed Li_2S_4 on the TiO_2–Ar surface is expected to decompose spontaneously and quickly,[70] leading to fast conversion kinetics.

To evaluate the redox kinetics of surface-adsorbed polysulfide species, Li adsorption on the TiO_2 (100) surface was also investigated. The results indicate that one preferential position for Li adsorption is located near the trigonal centre of 3 adjacent O atoms (Fig. S16a and b†). Such a configuration of Li adsorption *via* coordination with three O atoms gives a large E_{ad} of −4.43 eV. In contrast, the Li adsorption on the surface with $V_O^{\cdot}$ is similar to that of the pristine (100) surface, except for a subtle deviation of the trigonal centre possibly due to the lack of one coordinated O atom at the $V_O^{\cdot}$ position (Fig. S16c and d†). This also yields an E_{ad} of −3.63 eV. These large E_{ad} values of Li ion adsorption on the TiO_2 surface (without/with $V_O^{\cdot}$) suggest that Li can be concentrated on the TiO_2 (100) surface,[71] participating in the fast redox reaction of polysulfides during charge/discharge.

Next, the influence of $V_O^{\cdot}$ on the Li ion diffusion on the TiO_2 surface was further simulated. The calculated Li ion diffusion pathways on the pristine anatase (100) surface and surface with $V_O^{\cdot}$ are shown in Fig. S17† and 6, respectively. It depicts that Li ions can transport easily on the TiO_2 surface with a very low energy barrier of 0.145 eV (Fig. 6c). In comparison, the presence of $V_O^{\cdot}$ slightly impedes the Li ion diffusion surrounding $V_O^{\cdot}$ possibly due to the enhanced scattering of positively charged $V_O^{\cdot}$ towards Li ions. However, this value (0.293 eV) is smaller than that of some oxides and sulfides, such as SnO_2 (~1.0 eV)

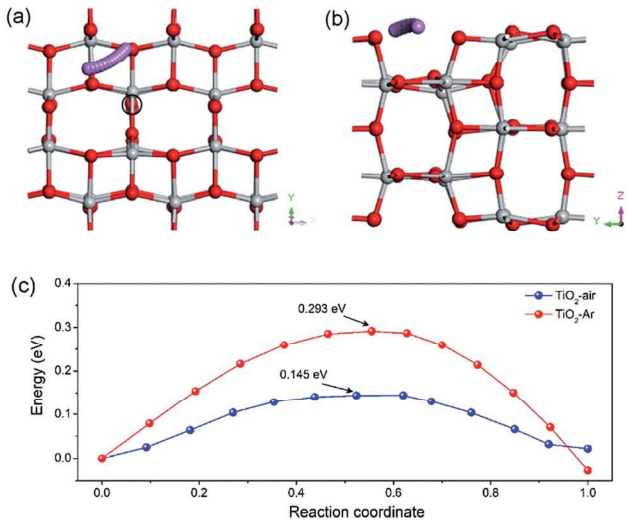

Fig. 6 Top (a) and side view (b) of Li diffusion on the anatase (100) slab surface and the corresponding energy profiles (c). The grey, red, and pink balls represent the Ti, O, and Li, respectively. The black circle in (a) signifies the $V_O^{\cdot\cdot}$ position.

and MoS_2 (~0.8 eV),[72] and Sb_2S_3 nanosheets (~0.31 eV).[73] The large electronic conductivity combined with high concentration of Li ions on the TiO_2 surface with large diffusivity ensures fast electrochemical redox conversion of polysulfides with fast kinetics,[67,72,73] which agrees well with electrochemical properties/performances shown in Fig. 4.

Conclusions

Oxygen-deficient TiO_2 has been successfully synthesized by a facile hydrothermal process combined with post annealing in Ar. Experimental data and DFT theoretical simulations reveal that the formation of oxygen vacancies ($V_O^{\cdot\cdot}$) effectively improves the electrical conduction in TiO_2 and enhances the binding of the TiO_2 surface to polysulfides. Meanwhile, Li ions can be concentrated and diffuse easily on the oxygen-deficient TiO_2 surface, propelling fast redox conversion kinetics of surface adsorbed polysulfides. When evaluated in Li–S cells, the TiO_2/S composite cathode delivers high capacity, outstanding rate capability and excellent cycling stability. The proposed vacancy engineering approach may pave the way for the rational design of novel sulfur host materials for high-performance Li–S batteries.

Conflicts of interest

There are no conflicts to declare.

Acknowledgements

This work is financially supported by the Basic Research Project of the Science and Technology Innovation Commission of Shenzhen (No. JCYJ20170817110251498), the Guangdong Special Support for the Science and Technology Leading Young Scientist (No. 2016TQ03C919), National Natural Science Foundation of China (51672230, 21603094), CityU Applied Research Grant (ARG 9667159), and in part by the National Science Foundation (No. 1803256). H.-E. Wang acknowledges the Hubei Provincial Department of Education for the "Chutian Scholar" program.

Notes and references

1 Q. Pang, X. Liang, C. Y. Kwok and L. F. Nazar, *Nat. Energy*, 2016, **1**, 16132.
2 Y.-X. Yin, S. Xin, Y.-G. Guo and L.-J. Wan, *Angew. Chem., Int. Ed.*, 2013, **52**, 13186–13200.
3 A. Manthiram, Y. Fu and Y.-S. Su, *Acc. Chem. Res.*, 2013, **46**, 1125–1134.
4 G. Li, S. Wang, Y. Zhang, M. Li, Z. Chen and J. Lu, *Adv. Mater.*, 2018, **30**, 1705590.
5 J. Sun, Y. Sun, M. Pasta, G. Zhou, Y. Li, W. Liu, F. Xiong and Y. Cui, *Adv. Mater.*, 2016, **28**, 9797–9803.
6 J. Park, B.-C. Yu, J. S. Park, J. W. Choi, C. Kim, Y.-E. Sung and J. B. Goodenough, *Adv. Energy Mater.*, 2017, **7**, 1602567.
7 Y.-S. Su and A. Manthiram, *Nat. Commun.*, 2012, **3**, 1166.
8 J. Liu, M. Sun, Q. Zhang, F. Dong, P. Kaghazchi, Y. Fang, S. Zhang and Z. Lin, *J. Mater. Chem. A*, 2018, **6**, 7382–7388.
9 G. Xu, Q.-b. Yan, A. Kushima, X. Zhang, J. Pan and J. Li, *Nano Energy*, 2017, **31**, 568–574.
10 W. Chen, T. Lei, C. Wu, M. Deng, C. Gong, K. Hu, Y. Ma, L. Dai, W. Lv, W. He, X. Liu, J. Xiong and C. Yan, *Adv. Energy Mater.*, 2018, **8**, 1702348.
11 S. Y. Lang, R. J. Xiao, L. Gu, Y. G. Guo, R. Wen and L. J. Wan, *J. Am. Chem. Soc.*, 2018, **140**, 8147–8155.
12 S. Wu, Z. Zhang, M. Lan, S. Yang, J. Cheng, J. Cai, J. Shen, Y. Zhu, K. Zhang and W. Zhang, *Adv. Mater.*, 2018, **30**, 1705830.
13 J. Xu, T. Lawson, H. Fan, D. Su and G. Wang, *Adv. Energy Mater.*, 2018, **8**, 1702607.
14 J. Park, S.-H. Yu and Y.-E. Sung, *Nano Today*, 2018, **18**, 35–64.
15 S. Rehman, K. Khan, Y. Zhao and Y. Hou, *J. Mater. Chem. A*, 2017, **5**, 3014–3038.
16 X. Ji, K. T. Lee and L. F. Nazar, *Nat. Mater.*, 2009, **8**, 500–506.
17 X. Li, Y. Cao, W. Qi, L. V. Saraf, J. Xiao, Z. Nie, J. Mietek, J.-G. Zhang, B. Schwenzer and J. Liu, *J. Mater. Chem.*, 2011, **21**, 16603–16610.
18 N. Jayaprakash, J. Shen, S. S. Moganty, A. Corona and L. A. Archer, *Angew. Chem., Int. Ed.*, 2011, **50**, 5904–5908.
19 F. Pei, T. An, J. Zang, X. Zhao, X. Fang, M. Zheng, Q. Dong and N. Zheng, *Adv. Energy Mater.*, 2016, **6**, 1502539.
20 (*a*) J. Cao, C. Chen, Q. Zhao, N. Zhang, Q. Lu, X. Wang, Z. Niu and J. Chen, *Adv. Mater.*, 2016, **28**, 9629; (*b*) X. Wang, Y. Li, T. Jin, J. Meng, L. Jiao, M. Zhu and J. Chen, *Nano Lett.*, 2017, **17**, 7989–7994; (*c*) X. J. Wang, K. Z. Cao, Y. J. Wang and L. F. Jiao, *Small*, 2017, **13**, 1700873.
21 M. Yan, H. Chen, Y. Yu, H. Zhao, C. F. Li, Z. Y. Hu, P. Wu, L. H. Chen, H. E. Wang, D. L. Peng, H. X. Gao, T. Hasan, Y. Li and B. L. Su, *Adv. Energy Mater.*, 2018, **8**, 1801066.
22 C. Tang, B. Q. Li, Q. Zhang, L. Zhu, H. F. Wang, J. L. Shi and F. Wei, *Adv. Funct. Mater.*, 2016, **26**, 577–585.

23 J. Zhang, C. P. Yang, Y. X. Yin, L. J. Wan and Y. G. Guo, *Adv. Mater.*, 2016, **28**, 9539.
24 Z.-L. Xu, J.-K. Kim and K. Kang, *Nano Today*, 2018, **19**, 84–107.
25 Z. B. Cheng, H. Pan, H. Zhong, Z. B. Xiao, X. J. Li and R. H. Wang, *Adv. Funct. Mater.*, 2018, **28**, 1707597.
26 X. Liang and L. F. Nazar, *ACS Nano*, 2016, **10**, 4192–4198.
27 X. Y. Tao, J. G. Wang, Z. G. Ying, Q. X. Cai, G. Y. Zheng, Y. P. Gan, H. Huang, Y. Xia, C. Liang, W. K. Zhang and Y. Cui, *Nano Lett.*, 2014, **14**, 5288–5294.
28 H. E. Wang, K. L. Yin, X. Zhao, N. Qin, Y. Li, Z. Deng, L. C. Zheng, B. L. Su and Z. G. Lu, *Chem. Commun.*, 2018, **54**, 12250–12253.
29 U. Zubair, J. Amici, C. Francia, D. McNulty, S. Bodoardo and C. O'Dwyer, *ChemSusChem*, 2018, **11**, 1838–1848.
30 Y. Zhang, Z. Mu, C. Yang, Z. Xu, S. Zhang, X. Zhang, Y. Li, J. Lai, Z. Sun, Y. Yang, Y. Chao, C. Li, X. Ge, W. Yang and S. Guo, *Adv. Funct. Mater.*, 2018, **28**, 1707578.
31 Z. B. Cheng, Z. B. Xiao, H. Pan, S. Q. Wang and R. H. Wang, *Adv. Energy Mater.*, 2018, **8**, 1702337.
32 S. Z. Huang, Y. Wang, J. P. Hu, Y. V. Lim, D. Z. Kong, Y. Zheng, M. Ding, M. E. Pam and H. Y. Yang, *ACS Nano*, 2018, **12**, 9504–9512.
33 X. C. Li, G. L. Guo, N. Qin, Z. Deng, Z. G. Lu, D. Shen, X. Zhao, Y. Li, B. L. Su and H. E. Wang, *Nanoscale*, 2018, **10**, 15505–15512.
34 C. Y. Fan, Y. P. Zheng, X. H. Zhang, Y. H. Shi, S. Y. Liu, H. C. Wang, X. L. Wu, H. Z. Sun and J. P. Zhang, *Adv. Energy Mater.*, 2018, **8**, 1703638.
35 C. Shang, L. Cao, M. Yang, Z. Wang, M. Li, G. Zhou, X. Wang and Z. Lu, *Energy Storage Materials*, 2019, **18**, 375–381.
36 L. B. Ma, H. Yuan, W. J. Zhang, G. Y. Zhu, Y. R. Wang, Y. Hu, P. Y. Zhao, R. P. Chen, T. Chen, J. Liu, Z. Hu and Z. Jin, *Nano Lett.*, 2017, **17**, 7839–7846.
37 Y. Z. Song, W. Zhao, L. Kong, L. Zhang, X. Y. Zhu, Y. L. Shao, F. Ding, Q. Zhang, J. Y. Sun and Z. F. Liu, *Energy Environ. Sci.*, 2018, **11**, 2620–2630.
38 Y. Zhong, D. L. Chao, S. J. Deng, J. Y. Zhan, R. Y. Fang, Y. Xia, Y. D. Wang, X. L. Wang, X. H. Xia and J. P. Tu, *Adv. Funct. Mater.*, 2018, **28**, 1706391.
39 X. X. Li, K. Ding, B. Gao, Q. W. Li, Y. Y. Li, J. J. Fu, X. M. Zhang, P. K. Chu and K. F. Huo, *Nano Energy*, 2017, **40**, 655–662.
40 Z. H. Li, Q. He, X. Xu, Y. Zhao, X. W. Liu, C. Zhou, D. Ai, L. X. Xia and L. Q. Mai, *Adv. Mater.*, 2018, **30**, 1804089.
41 C. Ye, Y. Jiao, H. Jin, A. D. Slattery, K. Davey, H. Wang and S.-Z. Qiao, *Angew. Chem., Int. Ed.*, 2018, 30325094.
42 H. Yuan, X. Chen, G. Zhou, W. Zhang, J. Luo, H. Huang, Y. Gan, C. Liang, Y. Xia, J. Zhang, J. Wang and X. Tao, *ACS Energy Lett.*, 2017, **2**, 1711–1719.
43 S. Z. Huang, Y. V. Lim, X. M. Zhang, Y. Wang, Y. Zheng, D. Z. Kong, M. Ding, S. Y. A. Yang and H. Y. Yang, *Nano Energy*, 2018, **51**, 340–348.
44 Z. W. Seh, W. Li, J. J. Cha, G. Zheng, Y. Yang, M. T. McDowell, P.-C. Hsu and Y. Cui, *Nat. Commun.*, 2013, **4**, 1331.
45 S. Evers, T. Yim and L. F. Nazar, *J. Phys. Chem. C*, 2012, **116**, 19653–19658.
46 G. Xu, Q.-b. Yan, S. Wang, A. Kushima, P. Bai, K. Liu, X. Zhang, Z. Tang and J. Li, *Chem. Sci.*, 2017, **8**, 6619–6625.
47 Y. Y. Li, Q. F. Cai, L. Wang, Q. W. Li, X. Peng, B. Gao, K. F. Huo and P. K. Chu, *ACS Appl. Mater. Interfaces*, 2016, **8**, 23784–23792.
48 M. Yu, J. Ma, H. Song, A. Wang, F. Tian, Y. Wang, H. Qiu and R. Wang, *Energy Environ. Sci.*, 2016, **9**, 1495–1503.
49 J.-Y. Hwang, H. M. Kim, S.-K. Lee, J.-H. Lee, A. Abouimrane, M. A. Khaleel, I. Belharouak, A. Manthiram and Y.-K. Sun, *Adv. Energy Mater.*, 2016, **6**, 1501480.
50 W. L. Wu, J. Pu, J. Wang, Z. H. Shen, H. Y. Tang, Z. T. Deng, X. Y. Tao, F. Pan and H. G. Zhang, *Adv. Energy Mater.*, 2018, **8**, 1702373.
51 X. T. Gao, Y. Xie, X. D. Zhu, K. N. Sun, X. M. Xie, Y. T. Liu, J. Y. Yu and B. Ding, *Small*, 2018, **14**, 1802443.
52 Z. Liang, G. Y. Zheng, W. Y. Li, Z. W. Seh, H. B. Yao, K. Yan, D. S. Kong and Y. Cui, *ACS Nano*, 2014, **8**, 5249–5256.
53 T. Xia, W. Zhang, J. B. Murowchick, G. Liu and X. B. Chen, *Adv. Energy Mater.*, 2013, **3**, 1516–1523.
54 Y. Wu, Y. Jiang, J. Shi, L. Gu and Y. Yu, *Small*, 2017, **13**, 1700129.
55 Y. Zhang, Z. Y. Ding, C. W. Foster, C. E. Banks, X. Q. Qiu and X. B. Ji, *Adv. Funct. Mater.*, 2017, **27**, 1700856.
56 C. Zhao, Y. Cai, K. Yin, H. Li, D. Shen, N. Qin, Z. Lu, C. Liu and H.-E. Wang, *Chem. Eng. J.*, 2018, **350**, 201–208.
57 Y. Wang, X. Xue, P. Liu, C. Wang, X. Yi, Y. Hu, L. Ma, G. Zhu, R. Chen, T. Chen, J. Ma, J. Liu and Z. Jin, *ACS Nano*, 2018, **12**, 12492–12502.
58 L. Kong, X. Chen, B. Q. Li, H. J. Peng, J. Q. Huang, J. Xie and Q. Zhang, *Adv. Mater.*, 2018, **30**, 1705219.
59 H. C. Wang, C. Y. Fan, Y. P. Zheng, X. H. Zhang, W. H. Li, S. Y. Liu, H. Z. Sun, J. P. Zhang, L. N. Sun and X. L. Wu, *Chem.–Eur. J.*, 2017, **23**, 9666–9673.
60 Y. Cai, H. E. Wang, S. Z. Huang, M. F. Yuen, H. H. Cai, C. Wang, Y. Yu, Y. Li, W. J. Zhang and B. L. Su, *Electrochim. Acta*, 2016, **210**, 206–214.
61 J. Chen, Z. Ding, C. Wang, H. Hou, Y. Zhang, C. Wang, G. Zou and X. Ji, *ACS Appl. Mater. Interfaces*, 2016, **8**, 9142–9151.
62 H.-E. Wang, X. Zhao, X. Li, Z. Wang, C. Liu, Z. Lu, W. Zhang and G. Cao, *J. Mater. Chem. A*, 2017, **5**, 25056–25063.
63 Y. Cai, H. E. Wang, X. Zhao, F. Huang, C. Wang, Z. Deng, Y. Li, G. Z. Cao and B. L. Su, *ACS Appl. Mater. Interfaces*, 2017, **9**, 10652–10663.
64 H.-E. Wang, X. Zhao, K. Yin, Y. Li, L. Chen, X. Yang, W. Zhang, B.-L. Su and G. Cao, *ACS Appl. Mater. Interfaces*, 2017, **9**, 43665–43673.
65 C. Zheng, S. Niu, W. Lv, G. Zhou, J. Li, S. Fan, Y. Deng, Z. Pan, B. Li, F. Kang and Q.-H. Yang, *Nano Energy*, 2017, **33**, 306–312.
66 M. Ben Yahia, F. Lemoigno, T. Beuvier, J.-S. Filhol, M. Richard-Plouet, L. Brohan and M.-L. Doublet, *J. Chem. Phys.*, 2009, **130**, 204501.
67 M. Wang, L. Fan, D. Tian, X. Wu, Y. Qiu, C. Zhao, B. Guan, Y. Wang, N. Zhang and K. Sun, *ACS Energy Lett.*, 2018, **3**, 1627–1633.
68 L.-C. Yin, J. Liang, G.-M. Zhou, F. Li, R. Saito and H.-M. Cheng, *Nano Energy*, 2016, **25**, 203–210.

69 X.-C. Liu, Y. Yang, J. Wu, M. Liu, S. P. Zhou, B. D. A. Levi, X.-D. Zhou, H. Cong, D. A. Muller, P. M. Ajayan, H. D. Abruna and F.-S. Ke, *ACS Energy Lett.*, 2018, **3**, 1325–1330.

70 F. X. Wu, T. P. Pollard, E. B. Zhao, Y. R. Xiao, M. Olguin, O. Borodin and G. Yushin, *Energy Environ. Sci.*, 2018, **11**, 807–817.

71 G. Y. Xu, Q. B. Yan, S. T. Wang, A. Kushima, P. Bai, K. Liu, X. G. Zhang, Z. L. Tang and J. Li, *Chem. Sci.*, 2017, **8**, 6619–6625.

72 G. Zhou, H. Tian, Y. Jin, X. Tao, B. Liu, R. Zhang, Z. W. Seh, D. Zhuo, Y. Liu, J. Sun, J. Zhao, C. Zu, D. S. Wu, Q. Zhang and Y. Cui, *Proc. Natl. Acad. Sci. U. S. A.*, 2017, **114**, 840–845.

73 S. Yao, J. Cui, J.-Q. Huang, Z. Lu, Y. Deng, W. G. Chong, J. Wu, M. I. U. Haq, F. Ciucci and J.-K. Kim, *Adv. Energy Mater.*, 2018, **8**, 1800710.